NDT&E International 145 (2024) 103137

Contents lists available at ScienceDirect

NDT and E International

journal homepage: www.elsevier.com/locate/ndteint

A coupled approach of spatial dielectric mapping and unsupervised machine learning for damage detection and severity segmentation in polymer matrix composites

Rishabh D. Guha [*,1,2], Katherine Berkowitz [1], Landon R. Grace [**]

Department of Mechanical and Aerospace Engineering, North Carolina State University, Engineering Building-III, 911 Oval Drive, Raleigh, NC-27606, USA

ARTICLE INFO

Keywords:
Dielectric characterization
Polymer-water interactions
Unsupervised clustering

ABSTRACT

The inevitable presence of moisture within a polymer composite has allowed for the development of a novel dielectric nondestructive evaluation (NDE) technique which capitalizes on the behavior of moisture under an applied electromagnetic field. Relative permittivity of water which is bound to the polymer network differ significantly from that of water which is not bound to the network, and the preferential diffusion of this "free" water to damage sites permits the creation of spatial permittivity maps. Presently, this technique has shown capability for damage detection but has not achieved quantification, which is crucial for industry use. The introduction of machine learning algorithms to existing techniques in this field has proven valuable, thus, a machine learning approach for data processing and damage quantification to the existing dielectric technique was developed and applied in this work. BMI/Quartz samples and S2-Glass/Epoxy samples were fabricated and subjected to impact damage via drop tower. The BMI samples were impacted centrally at 9 J and the S2-Glass samples were subjected to two impact events of differing energies, 5 and 3 J. An unsupervised K-means clustering algorithm was applied to the acquired dielectric scans at different gravimetric moisture contents which has provided promising results for all samples. Specifically, within the two impact samples, the algorithm assigned a higher cluster center to the site with more damage, indicating the technique has the capability to both detect and quantify impact damage at all moisture levels examined.

1. Introduction

Historically speaking, significant functional improvements in the engineering sectors has often been accompanied by breakthroughs at the frontier of materials discovery. In the aerospace and automobile industry, the development of fiber reinforced composites in the mid-twentieth century was one such event which led to rapid advances in terms of performance. When compared to conventional structural materials like steel, composites offer a higher strength to weight ratio [1,2], resistance to chemical contamination [3] and a higher thermal stability [4,5]. Composites also gained a lot of favor in the defense and military sectors when researchers discovered its ability to transmit radar signatures without considerable signal absorption [6]. The advantages this class of materials offer has led to a global composite market which was estimated at 86.4 billion USD in 2020. The industry is expected to expand at a compound annual growth rate (CAGR) of 6.6% from 2021 to 2028 [7].

Despite their obvious superiorities over existing material classes, it cannot be overlooked that the majority of applications where composites are employed are safety critical [8] where the failure of any constituent can trigger a catastrophic event without warning. Accurate damage detection and quantification in composites has been an active area of research for the past couple of decades [9–11] and the problem is complicated because, unlike metals, composites often do not show any visible signs of damage initiation or accumulation [12,13]. The multitude of applied loads and stresses from different sources during the operating lifetime makes it even more challenging to develop tools for residual life prediction [14,15]. Damage can initiate in a composite

* Corresponding author.
** Corresponding author.
E-mail addresses: rdguha@lbl.gov (R.D. Guha), lgrace2@ncsu.edu (L.R. Grace).
[1] The authors have contributed equally to this work.
[2] Present Address: Lawrence Berkeley National Laboratory, 1 Cyclotron Road, Berkeley, CA- 94720.

https://doi.org/10.1016/j.ndteint.2024.103137
Received 15 November 2023; Received in revised form 4 April 2024; Accepted 2 May 2024
Available online 3 May 2024

laminate from a seemingly benign event like a hail strike or a tool drop by an operator during a routine maintenance overhaul [16]. The barely visible matrix cracks generated will accumulate in-service as the structure is subjected to fluctuating cycles of temperature [17,18], freeze-thaw cycling [19,20], and fatigue loading [21–23]. Moreover, the polar nature of the polymer matrix of a composite coupled with exposure to low levels of precipitation or prolonged high humidity makes them amenable to low levels of moisture absorption [24,25]. Neat epoxy-based resins can absorb anywhere between 1 and 7% moisture by wt [26]. which can translate to a moisture content of ~3% by wt [27]. in a polymer composite. Earlier studies have provided a detailed documentation of the deleterious effect of absorbed moisture on the mechanical performance [28–32], thermal stability [33] and electrical insulation properties [34–36] of polymer matrix composites (PMC).

The combination of performance unpredictability, mechanical loads and environmental stressors makes it imperative to develop safe, reliable, and affordable methods of non-destructive evaluation (NDE) geared specifically for composites. Currently, there are a variety of available NDE techniques which aim to detect damage at different phases as it evolves in a composite [37–39]. The strengths and weaknesses of each technique have been discussed in previous review papers [40–43] but a persistent limitation across techniques is their inability to reliably predict sub-micron scale damage during the early lifetime of the composite. Some techniques like radiography [44] which perform well in the damage initiation phase are burdened by safety and economic restrictions. Consequently, despite the development of highly sophisticated NDE techniques at the academic level, a widespread adoption on the commercial scale is lacking and manual techniques that rely on operator skill like *'tap tests'* [45] are still prevalent.

We have briefly discussed the known degradation induced by moisture in composites, but some degree of absorption is inevitable even in low-humidity operating environments [46]. Molecular simulation studies [47–53] have demonstrated that the state of the ingressed water molecules is dependent on the intermolecular secondary bonding interactions with the polymer network and the physical morphology of the matrix. The presence of nanopores and voids can lead to local clusters of water molecules which do not engage in strong hydrogen bonds with the polar groups in the network. Spectroscopy [54–57] and dielectric relaxation [58,59] have been successful in identifying two distinct states of moisture in an epoxy – one which is clustered as water droplets ("free") and the other which is "bound" to the polymer matrix.

The presence of internal damage sites creates additional free volume in the form of microcracks where moisture can exist as "free" water and exhibit characteristics similar to bulk water [60–65]. In the case of dry non-conductive composites with fiberglass or quartz reinforcements, the composite laminates are considered homogenous with a relatively small disparity in terms of relative permittivity between fiber and matrix (both have a dielectric constant ~ 3) [66,67]. The dielectric properties of moisture are dependent on the dipolar rotational polarization mechanism under the influence of an applied electromagnetic field [68]. If the water molecules can align in the direction of the applied electromagnetic field, they have high relative permittivity. Hence bulk water has a significantly higher dielectric constant (~80) [69–71], creating a sharp contrast between the dielectric signatures of the "free" water and the composite phase. Water bound to the polymer network is significantly restricted in its motion and has a much lower dielectric constant of ~3.2 [36–72]. This means that even at very low levels of moisture absorption, the difference in dielectric constants between the free and bound water will cause localized rise in relative permittivity near the damage site. This phenomenon has been leveraged in a novel NDE technique where the different species of moisture have been used as an "imaging agent" to detect impact damage [60–74].

In the realm of composite NDE, the past few years have been underlined by the infusion of different machine learning (ML) algorithms to existing methodologies [75–81]. Since a major part of damage detection is identifying subtle changes in data patterns; applying ML enables a faster, more sophisticated, and reliable blueprint for determining the type, location, or extent of damage. For instance, Das et al. [77] used a one-class support vector machine (SVM) on the wave propagation data collected by piezoelectric transducers mounted on a cantilever carbon fiber composite beam. They were successful in detecting and classifying different forms of defects like holes, cuts, notches and delaminations in the samples. Jung et al. [79] developed nonlinear models for composite helicopter rotor blades and applied SVM to categorize damage into one of 'negligible', 'moderate' or 'severe' classes. Yuan et al. [80] adopted a deep learning approach and employed a unified Convolutional Neural Network (CNN)-Recurrent Neural Network (RNN) architecture to diagnose impact events from simulated wave fields on a finite element model.

The examples discussed above are applications of supervised ML which requires training on labeled data sets. But in many real-life scenarios it is hard to label the high-dimensional data extracted from NDE experiments. Unsupervised ML can be very useful in these cases for (i) **dimensionality reduction** (DR), projecting the high-dimensional data set into an easily interpretable two or three dimensional space and (ii) **clustering** which can detect patterns in unlabeled data and divide them into relevant subsets [82]. For instance, Park et al. [81] collected the in-situ electromechanical output during impact for carbon-fiber-reinforced plastic (CFRP). The seven-dimensional data was reduced to three dimensions using Principal Component Analysis (PCA) and unsupervised k-means clustering subsequently identified four different damage types in the sample. Liu et al. [76] analyzed the damage behaviors on composite wind turbine blades under accelerated fatigue loading and used bisecting k-means clustering on acoustic emission data to identify damage modes.

These works underscore the value of combining fundamental science with ML algorithms. Phenomenological differences in polymer-water interactions near the damage locations of fiberglass composites has already been well documented through near infrared (NIR) spectroscopy [62–64] and dielectric resonance [61–63]. This study aims to develop a damage quantification algorithm for non-conductive composites by applying unsupervised K-means clustering on spatial maps of relative permittivities. A damage mapping setup was used to track the localized changes in permittivity due to the presence of "free" water near the damage sites and unsupervised k-means clustering was used to divide the data into subsets of increasing damage. The algorithm was validated on Quartz/BMI samples with single impact locations. In these samples, the mapping setup worked as a damage detection technique which could accurately identify the location and the most affected area based on moisture induced permittivity changes. Post-validation, the setup was used for damage quantification in S-Glass/Epoxy samples with multiple locations of different impact energies. Finally, some future strategies are discussed which can help eliminate the current shortcomings of this methodology and enable its successful deployment in a commercial service setting.

2. Materials and methods

2.1. Materials

In this study, experiments were carried out on two different types of composite laminates. The validation was performed on quartz-reinforced BMI resin samples which had a single, centrally located impact site. The technique was then applied for damage quantification

Table 1
Average BMI/Quartz laminate properties.

Property	Average (%)	Standard Deviation (%)
Fiber volume percentage	59.41	0.149
Resin volume percentage	40.27	0.144
Void percentage	0.32	0.045

on three S-glass reinforced epoxy resin samples which had two impact sites with varying energies.

Two Quartz/BMI samples of approximate dimensions 132 mm × 75 mm (±5%) were cut with a wet diamond saw from a twelve-ply, 36 square inch laminate. The average sample thickness was 2.61 mm. This type of composite is typically employed in aircraft radomes and the BMI resin in the laminate has a commercial trade name of Hexcel® F650. The reinforcement is a woven eight-harness satin weave quartz fabric. It was cured at a US air force facility in an autoclave. A pre-cure conditioning was performed at 27 °C (80 °F) and 10 psi pressure for 30 min. The temperature was then raised to 190 °C (375 °F) at a rate of 3 °C (5 °F)/minute and was held constant at 85 psi pressure for 4 h. This was followed by a manufacturer recommended 8-h post-cure at 232 °C (450 °F) in which the temperature was increased at a maximum rate of 2 °C (3.3 °F).

The S2-glass/epoxy laminate was fabricated using a unidirectional prepreg consisting of a modified epoxy film adhesive matrix reinforced with AGY 463 S-2 Glass roving. A cross-ply laminate of size 304 mm × 304 mm was formed using 7 plies of prepreg, laid up in an alternating 0/90 sequence. The layup was then cured in a hot press at 345 kPa; it was heated from room temperature at an average rate of 10 °C/min until temperature reached 121 °C. Pressure and temperature were released after a cure time of 1 h, and the laminate cooled at an average rate of 2 °C/min until ambient temperature was achieved. A waterjet was used to cut three samples with dimensions 170 mm × 72 mm from the cured laminate and the average sample thickness was 2.167 mm (±1.8%).

The compositional properties were obtained through a high temperature resin burn-off in accordance with ASTM D3171 [83]. Pre-sample weights of 15 specimens for both the laminates were recorded and then they were maintained at 800 °C until the complete elimination of all the.

Resin. The post-burn weight allowed the accurate estimation of the resin, void and fiber percentages which have been recorded in Tables 1 and 2 respectively.

2.2. Sample Conditioning and impact setup

To ensure the elimination of any residual moisture, all the samples were dried in a vacuum oven at 65 °C in accordance with ASTM D5229 [84]. The sample weights were recorded on a high-precision Mettler-Toledo analytical balance. Since the percentage weight change during the conditioning can be as low as 0.03%, even static electrical charges on the surface of the specimen can trigger some spurious weight fluctuations. This effect was neutralized by applying pressurized air on the sample surface through an ionizing gun before recording the weight. After the weights stabilized, the samples were subjected to impact in a drop tower as shown in Fig. 1. The tower is equipped with a double column impactor guide mechanism and a hemispherical tip striker of radius 9.4 mm mounted on a crosshead. The payload has a total weight of 4.29 kg and the impact energies subjected on the samples can be modified by changing the drop height.

Low velocity out of plane impact of 9 J was applied at the center of the BMI/Quartz samples. In the case of the S2-glass/epoxy samples two locations were chosen along the central axis which were separated by 75 mm. These locations were subjected to impacts of 3 and 5 J respectively. Before impact, all the specimens were firmly secured between two 3 mm thick steel plates and the intended impact sites were exposed through a central cutout of 35 mm in the plates. The damage induced in the specimens was consistent with events like tool drops during maintenance or small hail strikes during service. As we can see in Fig. 2(a) and (b), they will be hard to detect especially if the panels are painted. These sites are examples of barely visible impact damage (BVID) which has minimal impact on the surface but is capable of internally initiating delaminations, matrix cracks and fiber breakage [85–87].

Table 2
Average Epoxy/S-glass laminate properties.

Property	Average (%)	Standard Deviation (%)
Fiber volume percentage	59.74	1.300
Resin volume percentage	35.46	1.032
Void percentage	4.80	0.880

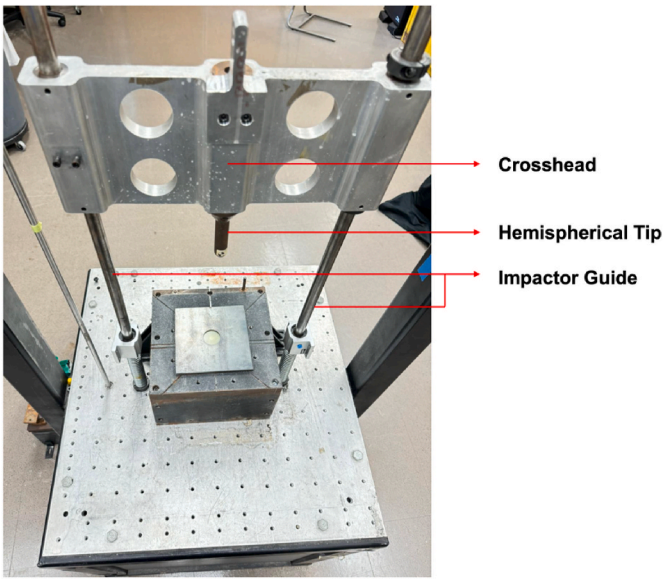

Fig. 1. Drop tower setup for inducing impact damage.

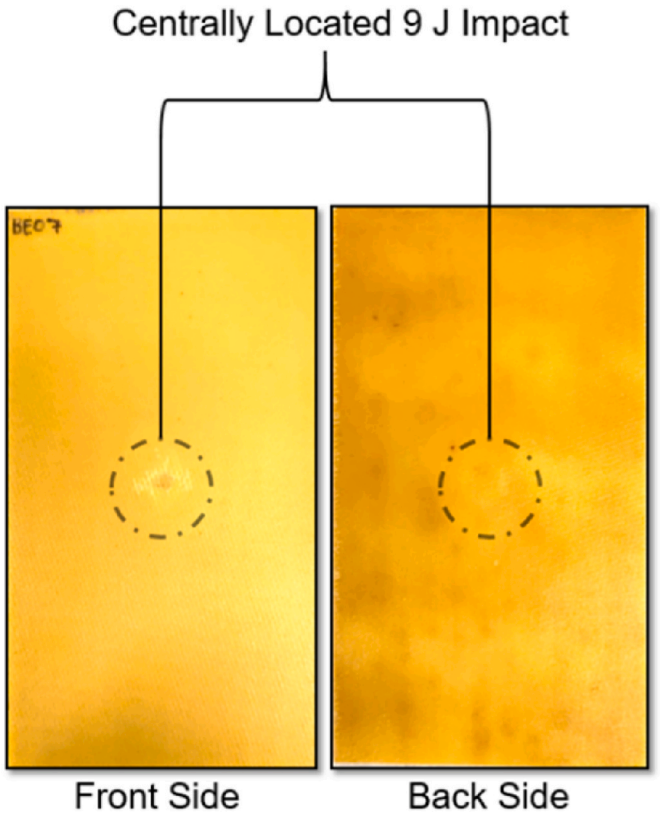

Fig. 2 (a). Front and Back side of one of the centrally impacted BMI/Quartz fiber samples.

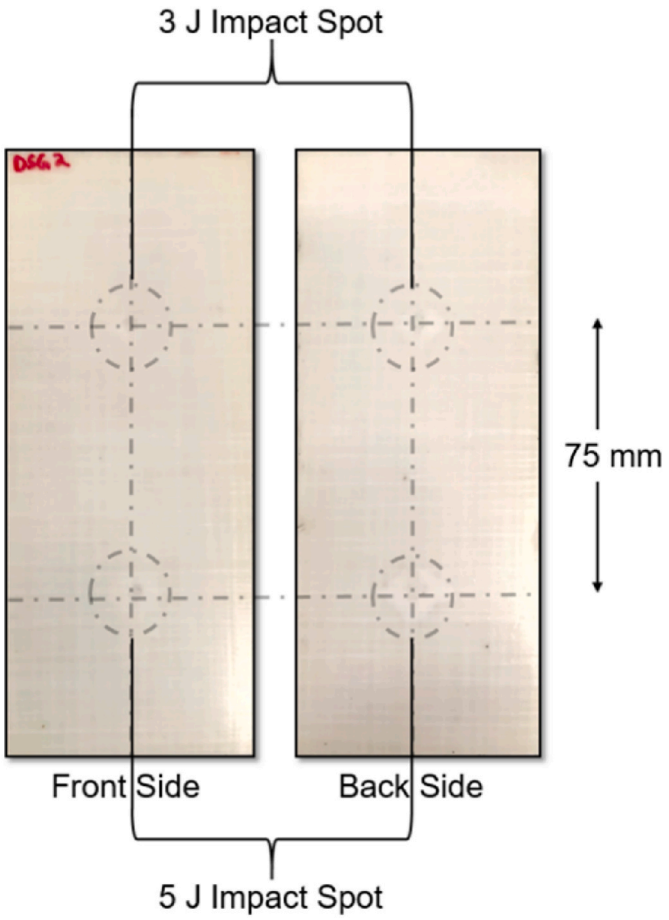

Fig. 2 (b). Front and Back side of one of the double impacted Epoxy/S-Glass samples.

2.3. Gravimetric moisture uptake

In previous studies the equilibrium moisture uptake level in BMI and epoxy resin composites have been found to be between 1.4 and 1.8% by wt [88,89]. But in this work, we explored the potential of damage detection and quantification at very low levels of moisture contamination and hence the maximum moisture uptake level tested in both classes of samples was ~0.4% by wt. Two separate approaches were adopted for conditioning the damaged samples which allowed us to replicate different in-service conditions. The BMI/Quartz samples were kept in a controlled humidity environment and their weight was monitored as they absorbed moisture from the ambient surroundings over a period of two months. On the other hand, the doubly impacted S-glass/epoxy samples were subjected to accelerated aging as they were submerged in a distilled water bath at a regulated temperature of 25 °C. These specimens were periodically removed from the bath and dried with a lint free cloth. Subsequently, they were allowed to stabilize in the lab conditions of ~60% humidity for 10 min before recording their weight. The uptake was calculated through the weight change of each sample according to:

$$M(\%) = \frac{W - W_i}{W_i} \times 100\% \quad (1)$$

where W is the weight of the specimen after absorption for a specific time and W_i is the initial, dry weight of the specimen after drying in the vacuum oven. The moisture uptake profile for all the three S-glass/epoxy samples have been included in Section 1 of the SI.

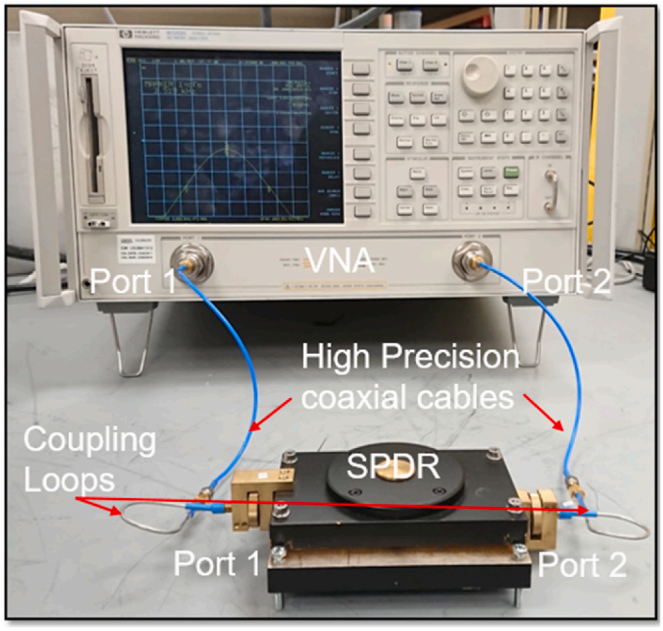

Fig. 3. Test Setup for measuring relative permittivity of composite samples.

2.4. Split post dielectric resonator and the damage mapping setup

The dielectric properties of the samples were recorded at a microwave frequency of 2.48 GHz using a split post dielectric resonator (SPDR) manufactured by QWED©, Poland [90,91]. The SPDR was coupled with an Agilent programmable Vector Network Analyzer (VNA) through high precision coaxial cables as seen in Fig. 3. This setup is capable of measuring bulk relative permittivity, and it can also track minute changes in relative permittivity (in the order of 10^{-3}). Prior calibration of the S-parameters (S11, S22 and S21) is necessary before using the equipment which is achieved by manually adjusting the coupling loops present at port 1 (S11) and port 2 (S22) until the loss in both signals are approximately equal. Consequently, both the loops are rotated in the opposite direction till the S21 signal loss becomes ~ -40 db. After the calibration is complete, the VNA is used to record the resonant frequency and quality factor (Q-factor) of the empty resonator.

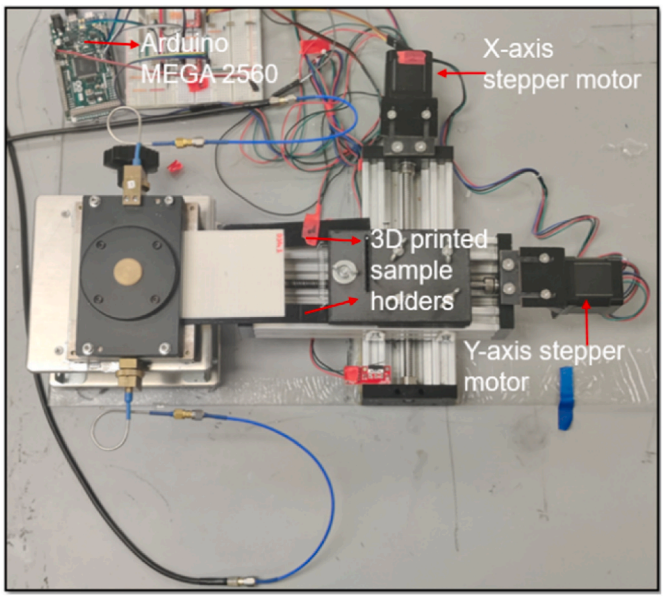

Fig. 4. Damage mapping setup for moving the specimen inside the SPDR.

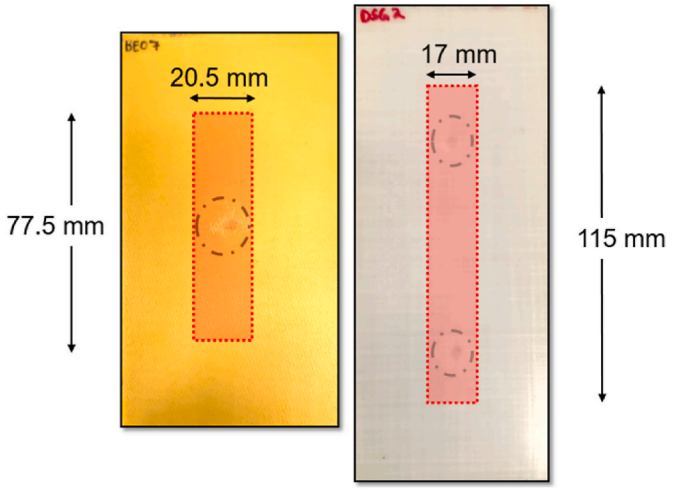

Fig. 5. Dimensions of scan area in (a) Quartz/BMI samples and (b) S-glass/epoxy samples.

The introduction of the sample shifts the resonant frequency of the SPDR, and the relative permittivity can be calculated from the difference in frequencies according to:

$$\varepsilon_r^{'} = 1 + \frac{f_0 - f_s}{h f_0 K_\varepsilon\left(\varepsilon_r^{'}, h\right)} \tag{2}$$

where f_0 is the empty resonator frequency, f_s is the SPDR frequency after the sample has been inserted, h is sample thickness and K_ε is a function of both $\varepsilon_r^{'}$ and h, the values of which are unique to each SPDR and provided in tabular form by the manufacturer.

The SPDR enables accurate permittivity measurements for the composite but in isolation, the device is restricted to single readings of the sample area which is encapsulated by the resonant cavity of the SPDR. For damage detection and quantification, a spatial map of permittivity measurements across the specimen dimensions is necessary. To achieve this goal, a custom damage mapping setup was devised with the help of stepper motors and microcontrollers. As seen in Fig. 4, NEMA-17 stepper motors were operated by A4988 motor drivers which could move the sample in both the x and y directions within the cavity. The drivers were controlled by an Arduino MEGA 2560 microcontroller board. Both the VNA and Arduino were interfaced through MATLAB® scripts allowing us to accurately move the samples with steps as low as 0.5 mm and trigger the VNA to take readings at individual sample points. The scan area had to be delineated in a manner which would guarantee that only the specimen was within the cavity for all the recorded observations. Scan dimensions higher than a certain prescribed limit would result in observations which are a combination of the sample and the 3-D printed holders within the cavity (see Fig. 4). Accounting for the dimensions of the SPDR cavity (55 mm diameter), the scan area was automatically calculated in the MATLAB script, and they have been shown for the Quartz/BMI and S-glass/epoxy samples in Fig. 5 (a) and (b) respectively.

2.5. Unsupervised K-means clustering

As discussed in the first section, machine learning can be an effective way of recognizing patterns in a data set and accelerate the accurate detection of damage modes in a composite. For instance, in a recent work, supervised learning was used on spatial dielectric maps at varying moisture concentrations [92]. The maps were superimposed on the images of the damaged samples which were part of the training set and points within the visible damage boundary were used to label the data. However, this technique has a few shortcomings. Firstly, it has an associated cost of exhaustive manual labeling and secondly, it is dependent on the external damage boundary and cannot account for unpredictable internal rupture mechanisms across different composite samples. In a real-life scenario, it is also possible that a data set trained on a particular group of samples does not translate well to a new sample. Therefore, this classification problem can greatly benefit from an unsupervised learning algorithm which can leverage patterns in unlabeled data and segment them into different heterogeneous groups based on the extent of damage. This task of discovering groups of similar attributes within the data set is called clustering and it comes with its own set of technical nuances worth noting. Since there are no external labels, it is difficult to know offhand how many clusters the data should be divided into. Concurrently, external validation or expert insight is necessary to interpret the veracity of the results generated by the model.

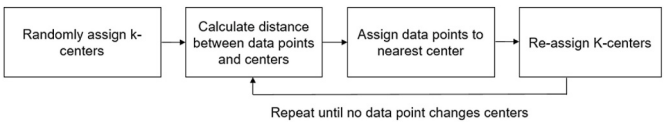

Fig. 6. A flowchart explaining the steps involved in K-means clustering.

K-means clustering is an example of an exclusive clustering algorithm which segments a given data set into a certain number of clusters k which is decided a-priori. The central idea of the algorithm is encapsulated in Fig. 6. One center is defined for each intended cluster and each point is assigned to the nearest centroids. Once all the points are assigned, the k centers are recalculated, and the process is iterated till the position of the centers become invariant. Similar to the supervised learning algorithms, K-means clustering also aims at minimizing the cost of an objective function which is defined by the squared error function as [88,89]:

$$J = \sum_{j=1}^{k} \sum_{i=1}^{x} \left\| x_i^{(j)} - c_j \right\|^2 \tag{3}$$

where $x_i^{(j)}$ are individual data points and c_j are the coordinates of the cluster centers. At the end of an iteration the new cluster centers are calculated from the reassigned points as:

$$c_j = \frac{1}{n_j} \sum_{j=1}^{n_j} x_i \tag{4}$$

where n_j represents the number of points in the jth cluster

The results from the algorithm are very sensitive to the initial assignments of the randomly assigned cluster centers and it does not always converge to the most optimal clustered segments. The probability of a non-optimum solution is higher when two cluster centers are initially assigned very close to one another. A solution to this problem is to use a smarter initialization technique which prioritizes greater distances from the initialized centers for the subsequent cluster centers. For instance, if one of the data points is randomly assigned as a cluster center c_k, then the distances of all the other non-selected data points are calculated from c_k. Then the next center is assigned to the data point (x_i) which maximizes the weighted probability distribution (P):

$$P = \frac{(x_i - c_k)^2}{\sum_{i=1}^{n} (x_i - c_k)^2} \tag{5}$$

K-means clustering performed after this initialization technique is called k-means ++ [93] and it dramatically improves the performance of the algorithm. In this work, the scikit-learn package in Python is used to execute the k-means algorithm which implements k-means ++ by default.

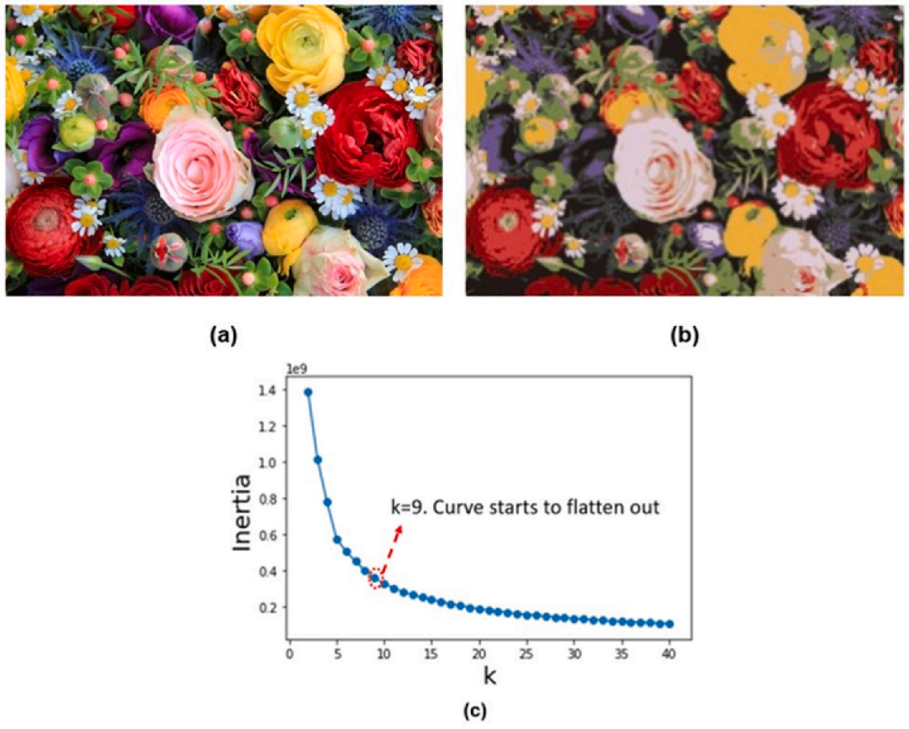

Fig. 7. Practical implementation of k-means clustering. (a) A high-resolution image (b) compressed image after clustering (c) inertia curve used to determine *k* from elbow method.

3. Results and discussion

3.1. Rationale for clustering

The inspiration behind using K-means clustering for segmenting the permittivity data into increasing levels of damage and delineating a damage boundary for the most affected area in the sample was taken from a comparable problem in image compression. Any computer image can be interpreted as a spatial map of pixels with 3 separate features capturing the red (R), blue (B) and green (G) signals. For example, in Fig. 7 (a), a bouquet of colorful flowers is represented by an image of 376 × 564 pixels. The multiple hues in the figure are due to the combination of thousands of unique colors. This image can be numerically unpacked as an array of 212,064 elements (283 × 407) with three feature vectors (RGB signals). If a K-means clustering algorithm is then applied to this array, the thousands of unique color shades can be clustered into a handful of color centers. When this array is again reshaped back into a pixelated image (see Fig. 7 (b)), the main features of the image are preserved despite having a significant loss in information. Each data point recorded during a dielectric scan can be likened to a pixel of an image as they also store information in the form of three feature vectors: permittivity values, loss tangent and signal bandwidth. Therefore, a spatial scan consisting of thousands of observations can be segmented into a few predefined damage levels (cluster centers). One of the challenges with this approach is to determine the optimal number of segments before executing the clustering algorithm. A possible solution to this problem is the 'elbow method', which uses a plot of inertia versus the number of clusters in the data set to determine the appropriate number of cluster centers. Inertia is defined as the sum of squared distance of each data point from its assigned cluster center. Increasing the number of clusters leads to a lower inertia due to the points becoming closer to a cluster center, but there is eventually a point at which we overfit the data and observe diminished returns. In the limiting scenario, the number of cluster centers will become equal to the number of data points resulting in zero inertia. The 'elbow method' attempts to find an inflection point on the plot after which the decrease in inertia slows down appreciably [94]. In some cases, it is hard to find a sharp inflection and the best possible candidate must be chosen from multiple options. Nine clusters were the chosen *k* for the image compression in Fig. 7 (b) which was selected from the inflection point seen in Fig. 7 (c).

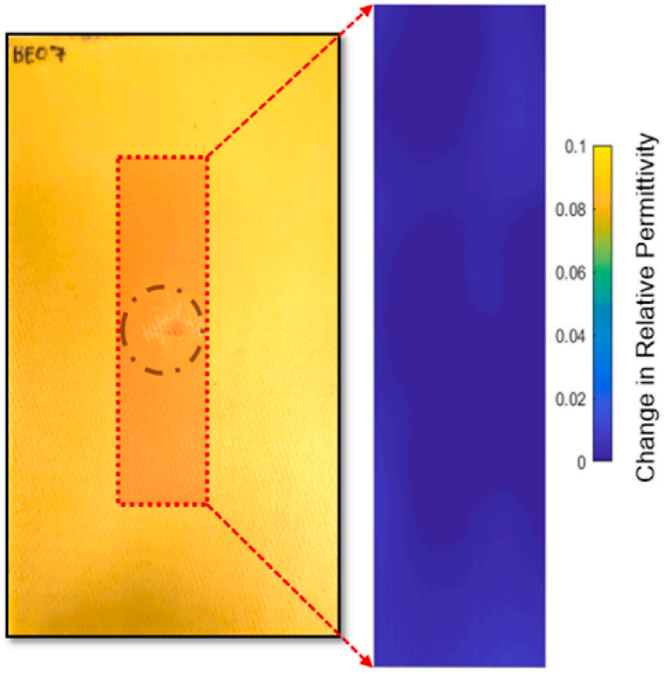

Fig. 8. Overall Invariance in permittivity in one of the damaged Quartz/BMI samples with 0% moisture (dry).

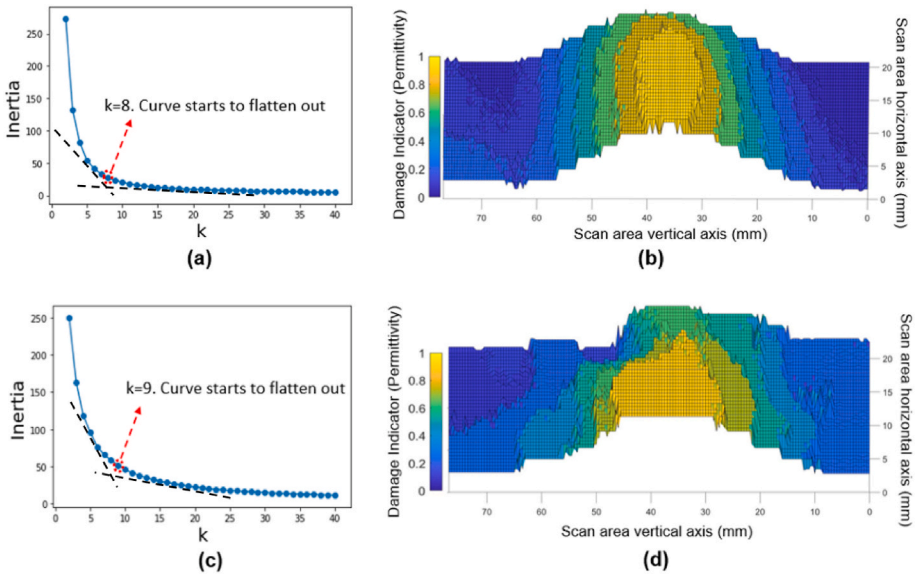

Fig. 9. (a) Inertia versus k curve for the first BMI sample at 0.2% moisture by wt. %. (b) Clustering results for the first Quartz/BMI sample at 0.2% moisture by wt. % (k = 8). (c) Inertia versus k curve for the first BMI sample at 0.16% moisture by wt. %. (d) Clustering results for the first Quartz/BMI sample at 0.16% moisture by wt. % (k = 9).

3.2. Validation in Quartz/BMI samples

It was critical to validate the damage detection technique and the clustering algorithm before applying it for damage quantification. Keeping that aim in mind, the two BMI samples were scanned in the dry state both before and after they had undergone impact at the drop tower. A fine step size of 0.5 mm was chosen in both the x and y directions which created a spatial map of 6355 data points. Then the permittivity variation between the dry pristine and damaged samples was evaluated. In accordance with our hypothesis of moisture induced rise in permittivity, there should not be any appreciable difference between the two scans, which is validated in Fig. 8 for one of the BMI samples. A similar figure for the other BMI sample is included in Section 2 of the SI. As mentioned in section 2.3, the Quartz/BMI samples were then exposed for ambient moisture absorption in a controlled humidity environment and periodic dielectric scans were taken at increasing moisture concentrations (by wt.%).

The dry scan of the damaged samples was chosen as the baseline which was subtracted from every scan conducted after moisture absorption. This was done to eliminate variation in permittivity due to thickness effects. The three feature vectors serving as damage indicators after the baseline subtraction were the differences in permittivity, loss tangent and bandwidth at each scan point respectively. The features had separate units and their respective variances also differed by orders of magnitude. Since K-means utilizes the squared distances between data points, the features with smaller variances will have a greater influence of the algorithm [95]. Therefore, the 6355 × 3 array was scaled in Python with a 'MinMaxScaler' available in the scikit-learn. preprocessing module and the resulting vectors were standardized indicators ranging between 0 and 1. Subsequently, the K-means algorithm was iteratively applied on the normalized arrays for each BMI sample and then reshaped back into the 155 × 41 two-dimensional spatial map obtained from the damaged samples. As seen in Fig. 9 (a) and (c), the elbow in the inertia curve occurred at approximately 8 and 9 clusters respectively. Fig. 9 (b) and (d) shows the results of the clustering in a three-dimensional contour plot using the scaled damage indicator for the permittivity variable. The segmentation creates envelopes of increasing damage as the scan moves towards the central impact location from either side. The trends of the damage are intuitive and can even be seen in contour maps of the raw data before it is passed through the k-means clustering algorithm. However, the segmentation resulting from the algorithm provides a much clearer and consistent picture of the exact damage boundary, irrespective of the moisture content. As seen when comparing the two figures, the damage boundary for each sample is different. This is a result of the unpredictability in the induced internal microcracks and delaminations in the separate composite samples despite similarities in constituents and damage history. In the first sample, the damage levels decrease almost concentrically with the

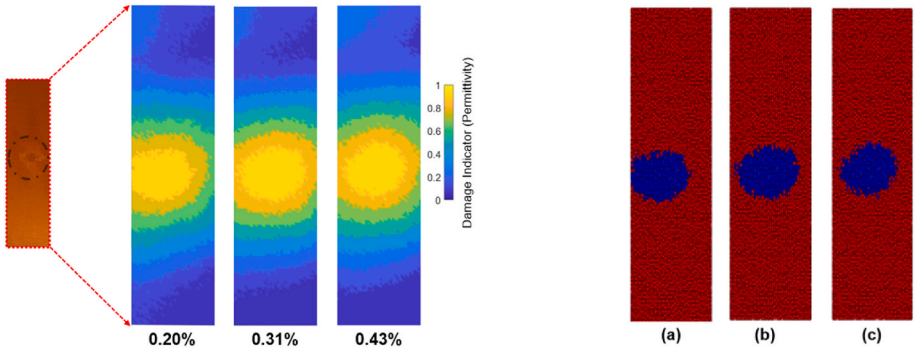

Fig. 10. Contour maps and labeled boundaries for the highest damage level in the scan area of the first Quartz/BMI sample at (a) 0.20% (b) 0.31% and (c) 0.43% moisture (by wt.%).

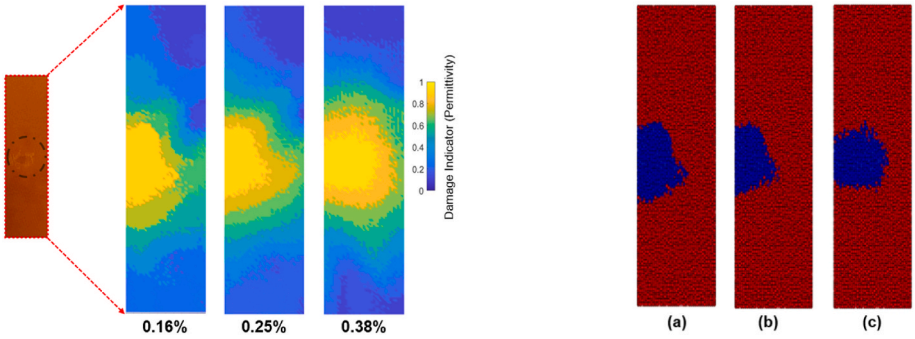

Fig. 11. Contour maps and labeled boundaries for the highest damage level in the scan area of the second Quartz/BMI sample at (a) 0.16% (b) 0.25% and (c) 0.38% moisture (by wt.%).

highest indicated damage at the center of the scan area. Observations in the second sample convey that the damage is shifted to the edge of the scan area and the boundary is broader for the highest damage level. It is possible that the induced damage from the drop tower was slightly off-center in the second sample. The ability of the algorithm to catch such subtle differences in BVID profiles at moisture contents as low as 0.2% and 0.16% by wt. makes the technique very promising when compared to the lower resolutions of ultrasonic C-scans [96]. Figs. 10 and 11 compare the damage maps of the two samples at increasing moisture.

Concentrations. Companion figures were also obtained from Python by labeling all the data points in the highest damage level as 1 and every other point as 0. These binary figures help to delineate the boundaries for the most affected regions in the samples at different moisture concentrations. The chosen value of k (8 and 9) was kept constant for both the samples even as the moisture concentration increased. The overall consistency in the detected damage areas also shows that the algorithm can account for the elevation in overall permittivity due to a rise in moisture content.

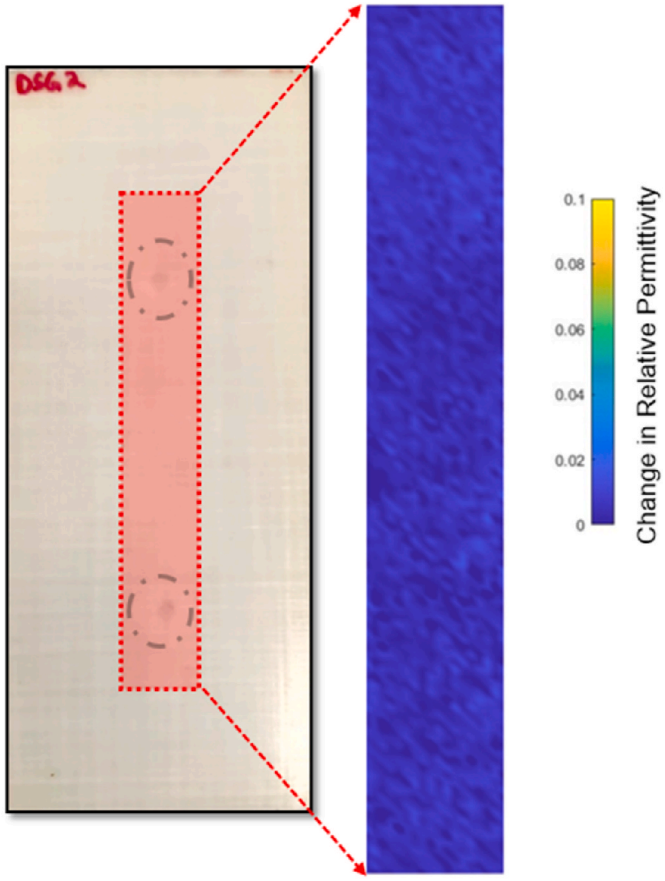

Fig. 12. Overall Invariance in permittivity in one of the damaged S-glass/Epoxy samples with 0% moisture (dry).

3.3. Damage quantification in S-glass/epoxy samples

The results of the previous sub-section clearly show that the spatial dielectric mapping coupled with the k-means clustering algorithm can help detect the BVID location in composite samples. But the possibility of applying this technique to quantify the extent of damage is still unexplored. For this purpose, the S-glass/epoxy samples with two damage sites of varying impact energies (3 J and 5 J) were periodically scanned at specific moisture contents. Like the BMI samples, the scan at 0% moisture for the damaged samples was subtracted as a dry baseline from every subsequent wet scan. A difficulty with these experiments was the loss in moisture content during the scan process. Since the scan dimensions of these samples was larger, the scanning time of each sample at a 0.5 mm step size was considerably longer than the BMI samples. Each scan at 0.5 mm step size took approximately 11 h and as these samples were conditioned in a water bath, there was a loss of moisture content during the scan due to the ambient exposure. To mitigate this issue, a step size of 1 mm was chosen in both the x and y directions and the MATLAB® 'interp' command was used to linearly interpolate the missing value between any two successive data points. As we have already seen [97], the loss in scan accuracy is minimal for small changes in step sizes. Consequently, a spatial map of 2088 (116 × 18) data points was interpolated to get a refined data set of 8085 (231 × 35) points, while cutting down the scan time to approximately 4.5 h. The overall permittivity invariance in the dry state for one of the S-Glass/Epoxy samples is shown in Fig. 12 and similar figures for the remaining two samples have been included in Section 3 of the SI.

Dielectric scans were taken at increasing moisture contents of 0.05% by wt. starting from a moisture concentration of 0.05%. The same normalization technique used for the BMI samples was utilized to scale the feature vectors. When the clustering algorithm was applied on these samples, all the three exhibited an elbow in the inertia curve at approximately $k = 10$. The plot for one of the samples is shown in Fig. 13 (a) and similar plots for the other two samples have been included in Section 4 of the SI. Due to the multiple impact spots, two different elevated damage segments are expected and as we can see in Fig. 13 (b), separate envelopes near the respective impact locations are observed. A narrow strip of damage is also detected at the center of the sample where no external impact was applied. We suspect that this is due to a 'knock-on' effect from the double impacts separated by a narrow spatial margin of 75 mm. The consecutive impact events might have induced coupled cracks along some of the in-axis laminas. If further validation corroborates this hypothesis, then it also vindicates the use of this method for tracing composite damage progression from associated loads. A

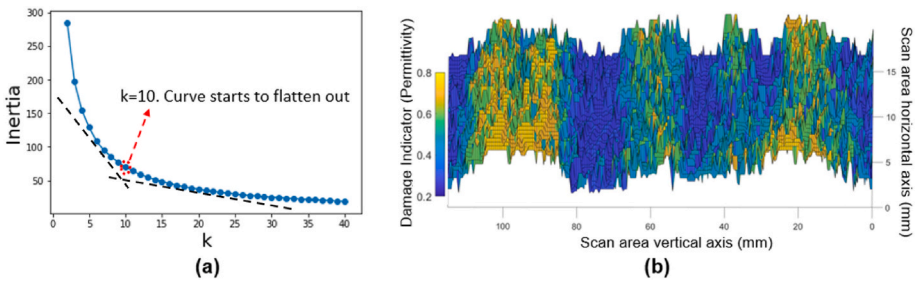

Fig. 13. (a) Inertia versus k curve for the first S-Glass/Epoxy sample at 0.05% moisture by wt. %. (b) Clustering results for the first S-Glass/Epoxy sample at 0.05% moisture by wt. % (k = 10).

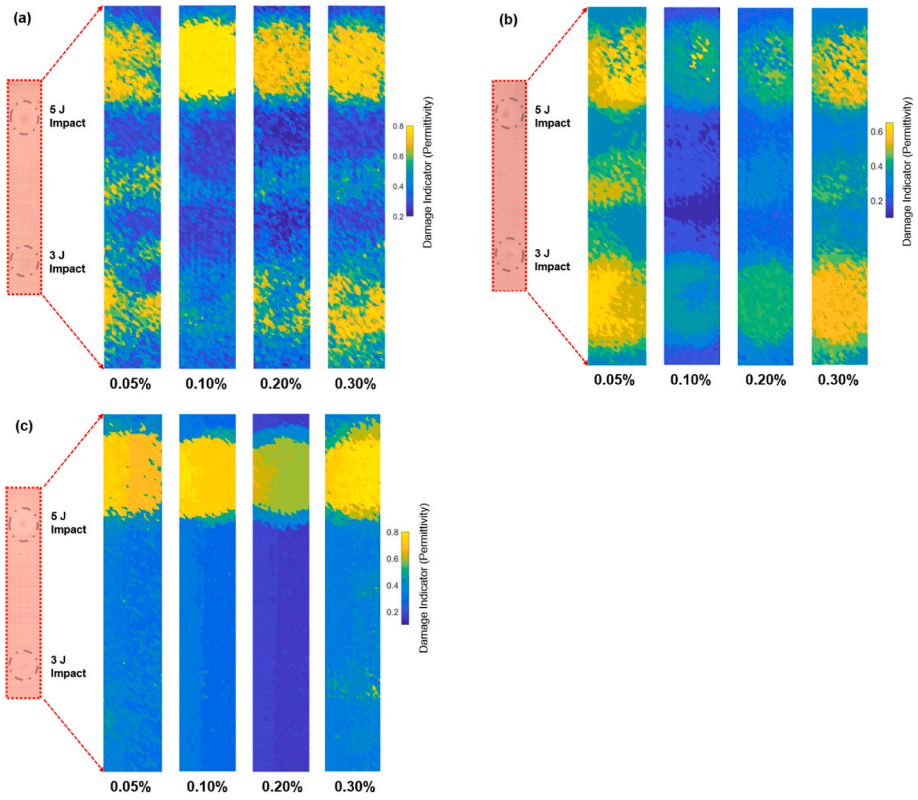

Fig. 14. (a)-(c) Contour maps after clustering showing the damage boundaries in the 3 multi-impacted S-Glass/Epoxy samples at (i) 0.05% (ii) 0.10% (iii) 0.20% and (iv) 0.30% moisture concentration (by wt.).

comparative analysis with Fig. 12 makes the results in Fig. 13 (b) particularly encouraging since they are obtained at a moisture concentration as low as 0.05% (by wt.).

Fig. 14 (a), (b) and (c) illustrates the damage maps of the three S-glass/Epoxy samples at increasing moisture concentrations ranging from 0.05% to 0.30% moisture (by wt.). A couple of additional scans for each sample at 0.15% and 0.25% by wt. have been included in Section 5 of the SI. For the first two samples, the clustering not only detects the two impact spots clearly, it also performs well with respect to quantifying the difference in extent of damage within the.

Sample. In Fig. 14 (a), across all the moisture concentrations, the 5 J impact spot has a wider coverage of the highly damaged clusters when compared to the 3 J impact spot. This indicates an overall moisture distribution across the sample with a higher concentration of free water near the.

5 J damage site triggered by a greater availability of microcracks, voids and delaminations. The narrow strip of elevated damage near the center of the sample also persists in every scan of Figure.

14 (a) and as mentioned earlier, this might be because of additional in-axis cracks induced in some of the laminas through consecutive impacts. Although more uniform in terms of damage distribution, the second sample (Fig. 14 (b) also exhibits small pockets of higher damage near the 5 J damage site. In case of the third sample (Fig. 14 (c)), the 3 J impact site is not clearly detected in all the scans at different moisture concentrations. At the lowest and highest moisture contents of 0.05% and 0.30% by wt., a faint damage boundary is detected near the site. Since the technique worked for the other two samples, it is improbable that clustering was unsuccessful in segmenting the envelope created by the 3 J damage. A more likely explanation is that the 3 J drop did not induce damage which is discernible at lower moisture concentrations which again highlights the unpredictability associated with low energy impact events.

The highest and the second highest damage envelopes in these samples were labeled in Python after clustering and the results for 0.30% moisture by wt. has been summarized in Fig. 15 (a)-(c). The higher density of 'Damage Level 1' labeled points for all the samples near the 5 J impact site reinstates the promise of this approach for comparing and quantifying multiple BVID sites in the same composite sample.

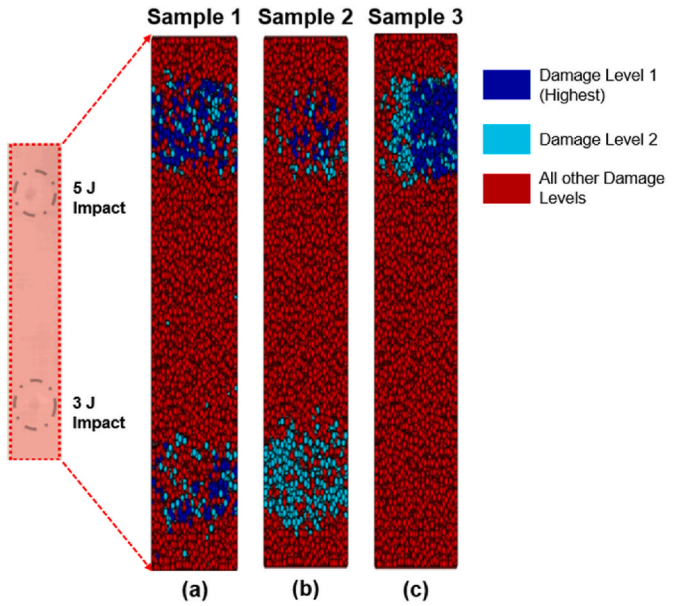

Fig. 15. (a)-(c) Labeled damage maps showing the two most affected damage envelopes in all the S-glass/Epoxy samples at 0.30% moisture content by wt.

3.4. Limitations and future directions

The results compiled in this work are strong pointers to remain optimistic about leveraging the duality in dielectric properties of absorbed moisture; not only as an imaging agent for detection, but also for quantification of the extent of sub-micron scale internal damage in a safety-critical composite structure. Despite the promising signs, there are still some strides to be made before this technique can be deployed on a commercial scale.

The first hurdle which needs to be overcome is the limitations in terms of sample dimensions. Since the SPDR is a compact device, we are currently limited to relatively small samples with a maximum thickness of ~3 mm. In a field scenario, besides being much larger, the composite panels would also be part of a much bigger structure which cannot be maneuvered inside a SPDR cavity. A potential solution is to use other dielectric techniques which are not spatially confined, such as the free-space method which uses coupled spot focusing antennas [98,99] to replace the function of the SPDR cavity. The free-space technique has been previously used for the NDE of composite materials [100]. Another alternative would be to use other characterization techniques which could quantify the relative concentration of free and bound water. Previous works have demonstrated [64–101] that Near Infrared (NIR) Spectroscopy can evaluate the free to bound water ratio in damaged composite samples and future work is underway for a similar damage mapping setup with a Nano NIR scanner [102] which can map the water states distribution across a damaged sample. The scanner also eliminates the thickness restrictions imposed by the SPDR cavity. Further, it is a single-sided access method as opposed to double-sided (as the current dielectric techniques are) and expands the usage possibilities to structures which cannot be accessed from both sides.

The efficiency of this technique currently pales in comparison to other common NDE methods; at this stage of development, mapping a large composite panel would take days. Moreover, since the method is dependent on the moisture concentration in the sample, the associated moisture loss during a prolonged scan can lead to inaccurate damage maps. We attempted to minimize the moisture loss during scans by using a humidifier inside the lab and we are currently working on establishing a better understanding between scan resolution and accuracy to optimize the method [97]. Preliminary results have shown that the loss in scan accuracy is minimal if a finer damage map is interpolated from a coarser step size. Establishing an optimal scan resolution which balances the tradeoffs between accuracy and speed will significantly accelerate the scanning process.

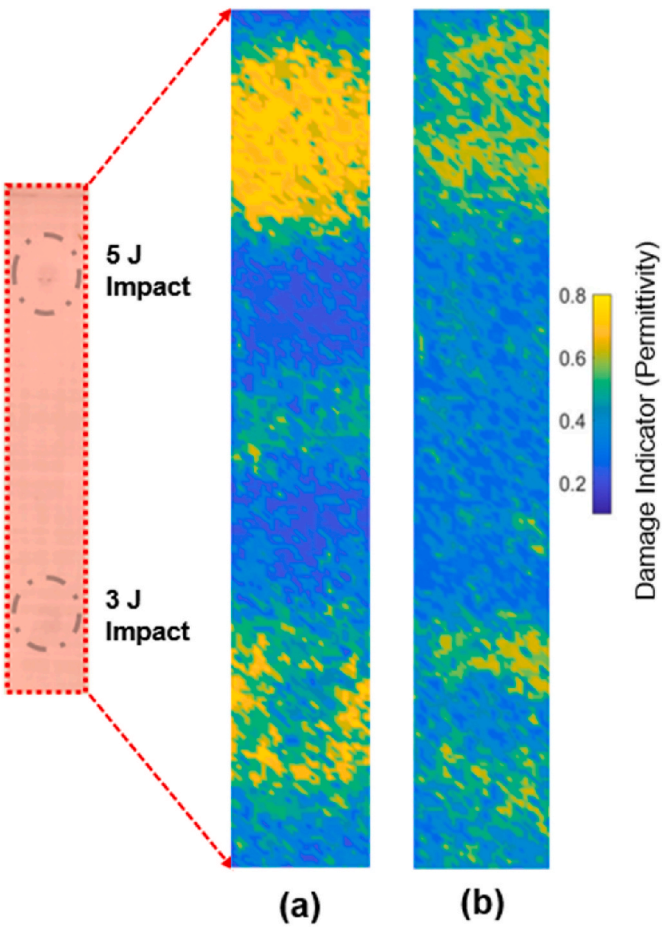

Fig. 16. Contour Maps delineating the damage boundaries in the first S-Glass/Epoxy sample at 0.20% moisture by wt. using (a) the dry sample as the baseline (b) the scan at 0.05% moisture as the baseline.

The necessity of a dry baseline subtraction from the scan also complicates this NDE method, especially in a commercial setting where the moisture content in a given sample will be unknown. It would be an impractical, if not impossible, approach for most structures to dry every component of interest for days and then re-expose them to ambient moisture. But further investigations of our technique have evidenced that this shortcoming can be mitigated by taking two scans with moisture contamination and subtracting the scan at the lower moisture content as the baseline. As seen in Fig. 16 (b), the sample 1 damage maps obtained after using the scan at 0.05% moisture concentration as the baseline yields comparable results to Fig. 16 (a) where the dry baseline is used. In a service setting, two consecutive scans with one at a relatively higher moisture content should eliminate the need of a dry baseline scan.

The characterization is also restricted to fibers and matrices which are non-conductive. Since the polarization tendencies in these materials are overshadowed by conduction, the dielectric properties cannot be effectively measured [103]. This limitation can be partially overcome by using NIR as the characterization tool, but even then, some reinforcements with strong absorbance (carbon fiber) can reduce the sensitivity and overall effectiveness of damage detection. However, given the widespread use of glass fibers, this technique can still be leveraged for industry use.

Finally, although there are very few existing techniques with capabilities to accurately detect damage at the sub-micron scale, the

proposed method in this work would benefit from some validation through available characterization tools, especially if they can visually corroborate the actual damage boundaries with the envelopes formed by the clustering algorithm. Current work is underway which aims to compare the results of dielectric mapping with reconstructed, ply-level, three dimensional images from x-ray computed tomography (CT). X-ray CT coupled with image analysis is very adept at quantitatively characterizing sub-micron scale damage but the radiation concerns associated with its use limits its adoption in a service setting.

4. Conclusions

Previous studies have illustrated the differences in the physical states and chemical interactions of absorbed moisture in the damaged and undamaged regions of a fiber reinforced polymer matrix. This phenomenological duality, coupled with the power of unsupervised clustering was leveraged to develop a damage detection and quantification technique for non-conductive composite materials. An attempt was made to cover a range of available polymer matrix composites (PMC). To achieve this goal, samples were procured from 12 ply woven Quartz/BMI panel and 7 ply unidirectional (cross ply) S-glass/epoxy laminates. Barely Visible Impact Damage (BVID) of 9 J was centrally applied on the BMI samples and the specimens were exposed to ambient moisture for a period of two months during which they reached a maximum moisture content of ~0.40% by wt. On the other hand, two impact sites of 3 J and 5 J was induced in the epoxy samples, and they were subjected to accelerated absorption of up to 0.30% by wt. by submerging them in a temperature-controlled water bath. Unsupervised K-means clustering was applied to periodic spatial scans of relative permittivity at increasing moisture concentrations obtained using an SPDR with a microwave resonant frequency (2.481 GHz). In the BMI samples, the processed results showed that the technique can not only be accurately used for damage detection, but it can also segment the scanned data into levels of increasing damage. The algorithm was subsequently extended for damage quantification in the epoxy samples which had multiple damage sites with differing impact energies (3 J vs 5 J). The technique was successful in identifying both the affected areas and quantitatively; it consistently assigned a comparatively higher cluster center to the 5 J site.

The process of combining clustering with the spatial variation in the states of absorbed moisture has the potential to be developed into an efficient damage quantification methodology which also produces interpretable and accurate results. Some current shortcomings hinder its widespread commercialization but possible solutions for overcoming those limitations have been discussed in the current work and will continue to be active topics of research in future studies.

CRediT authorship contribution statement

Rishabh D. Guha: Conceptualization, Data curation, Formal analysis, Investigation, Methodology, Software, Validation, Visualization, Writing – original draft, Writing – review & editing. **Katherine Berkowitz:** Data curation, Methodology, Validation, Writing – original draft, Writing – review & editing. **Landon R. Grace:** Conceptualization, Funding acquisition, Investigation, Project administration, Resources, Supervision, Writing – original draft, Writing – review & editing.

Declaration of competing interest

The authors declare that they have no known competing financial interests or personal relationships that could have appeared to influence the work reported in this paper.

Data availability

Data will be made available on request.

Acknowledgements

This material is based upon work partially supported by the National Science Foundation (NSF) - US. under Grant Number: CMMI-175482.

Appendix A. Supplementary data

Supplementary data to this article can be found online at https://doi.org/10.1016/j.ndteint.2024.103137.

References

[1] Bakhshi B, Heydarian M. Study of mechanical, flame, and water stability of phenolic resin/carbon fiber/nanosilica composites. Polym Compos 2021;42(8):3892–8. Available: https://doi-org.prox.lib.ncsu.edu/10.1002/pc.26101.
[2] Steinke K, Groo L, Sodano HA. Laser induced graphene for in-situ ballistic impact damage and delamination detection in aramid fiber reinforced composites. Compos Sci Technol 2021;202:108551. Available: https://www-sciencedirect-com.prox.lib.ncsu.edu/science/article/pii/S0266353820323435.
[3] Kim K, et al. Enhanced physical stability and chemical durability of sulfonated poly(arylene ether sulfone) composite membranes having antioxidant grafted graphene oxide for polymer electrolyte membrane fuel cell applications. J Membr Sci 2017;525:125–34. Available: https://www-sciencedirect-com.prox.lib.ncsu.edu/science/article/pii/S0376738816312650.
[4] Wang Y, Qiu X, Zheng J. Study the mechanism that carbon nanotubes improve thermal stability of polymer composites: an ingenious design idea with coating silica on CNTs and valuable in engineering applications. Compos Sci Technol 2018;167:529–38. Available: https://www-sciencedirect-com.prox.lib.ncsu.edu/science/article/pii/S0266353818312971.
[5] J. Guo et al., "Thermal stability and thermal degradation kinetics of short and long glass fiber reinforced PA10T composites," Polym Eng Sci, vol. 59, (2), pp. 246-253.
[6] Loss KR. Damage tolerant sandwich panel core with low moisture affinity. In: Proceedings of American Society for composites 29th technical conference on composite materials; 2014.
[7] Anonymous (.). Composites market size, share & trends analysis report by product (carbon, glass), by resin (thermosetting, thermoplastics), by manufacturing process, by end use, and segment forecasts. https://www.grandviewresearch.com/industry-analysis/composites-market; 2020 - 2027.
[8] Kaware K, Kotambkar M. Low velocity impact response and influence of parameters to improve the damage resistance of composite structures/materials: a critical review. Int J Crashworthiness 2021:1–25.
[9] Cantwell WJ, Morton J. The significance of damage and defects and their detection in composite materials: a review. J Strain Anal Eng Des Jan 01, 1992;27(1):29–42.
[10] Raut NP, Kolekar AB, Gombi SL. Methods of damage detection on composites under low velocity impact: review. Mater Today Proc Jan 01, 2020, 2019;27:2823–7.
[11] Yuan FG. Structural health monitoring (SHM) in aerospace structures. Woodhead Publishing; 2016.
[12] Vaidya UK. Impact response of laminated and sandwich composites. In: *Impact Engineering of composite Structures*Anonymous; 2011. p. 97–191.
[13] Hakim S, Razak HA. Adaptive neuro fuzzy inference system (ANFIS) and artificial neural networks (ANNs) for structural damage identification. Struct Eng Mech: Int J 2013:779–802.
[14] Sakin R, Ay İ. Statistical analysis of bending fatigue life data using Weibull distribution in glass-fiber reinforced polyester composites. Materials in Engineering 2008;29(6):1170–81.
[15] Feng Y, et al. Reliability fatigue life and A new S–N curve model of composite laminates under tensile-tensile fatigue load. Appl Compos Mater Feb 01, 2021;28(1):129–48.
[16] Hull D, Shi YB. Damage mechanism characterization in composite damage tolerance investigations. Compos Struct 1993;23(2):99.
[17] Gude MR, Prolongo SG, Ureña A. Hygrothermal ageing of adhesive joints with nanoreinforced adhesives and different surface treatments of carbon fibre/epoxy substrates. Interntaional Journal of Adhesion and Adhesives 2013;40:179–87.
[18] Jiang X, Kolstein H, Bijlaard FSK. Moisture diffusion in glass–fiber-reinforced polymer composite bridge under hot/wet environment. Composites. Part B, Engineering Feb 01, 2013;45(1):407–16.
[19] Shi J, et al. Bond behavior between basalt fiber–reinforced polymer sheet and concrete substrate under the coupled effects of freeze-thaw cycling and sustained load. J Compos Construct 2013;17(4).
[20] Shi J, et al. Tensile behavior of FRP and hybrid FRP sheets in freeze–thaw cycling environments. Composites. Part B, Engineering Apr, 2014;60:239–47.
[21] Califano A, Grassia L, D'Amore A. Fatigue of composite materials subjected to variable loadings. J Mater Eng Perform Oct 01, 2019;28(10):6538–43.
[22] Giancane S, Panella FW, Dattoma V. Characterization of fatigue damage in long fiber epoxy composite laminates. Int J Fatig 2010;32(1):46–53.
[23] D'Amore A, Grassia L. A method to predict the fatigue life and the residual strength of composite materials subjected to variable amplitude (VA) loadings. Compos Struct 2019;228(August):111338.

[24] Ellyin F, Rohrbacher C. The influence of aqueous environment, temperature and cyclic loading on glass-fibre/epoxy composite laminates. J Reinforc Plast Compos Jan 01, 2003;22(7):615–36.
[25] Schutte CL. Environmental durability of glass-fiber composites. Mater Sci Eng R Rep 1994;13(7):265.
[26] Soles CL, Yee AF. A discussion of the molecular mechanisms of moisture transport in epoxy resins. J Polym Sci B Polym Phys 2000;38(5):792.
[27] Zhang R, et al. Investigation into thinning and spring back of multilayer metal forming using hydro-mechanical deep drawing (HMDD) for lightweight parts. Int J Adv Manuf Technol 2016;82(5–8):817–26.
[28] Dhakal HN, Zhang Z. Polymer matrix composites: moisture effects and dimensional stability. Wiley Encyclopedia of Composites; 2012. p. 2179–85.
[29] Theocaris PS, Kontou EA, Papanicolaou GC. The effect of moisture absorption on the thermomechanical properties of particulates. Colloid Polym Sci May, 1983; 261(5):394–403.
[30] Jones FR, Foreman JP. 12 - the response of aerospace composites to temperature and humidity. In: *Polymer Composites in the aerospace Industry*Anonymous. Elsevier Ltd; 2015. p. 335–69.
[31] Grace LR, Altan MC. Characterization of anisotropic moisture absorption in polymeric composites using hindered diffusion model. Compos Appl Sci Manuf Aug 01, 2012;43(8):1187–96.
[32] Grace LR, Altan MC. Non-fickian three-dimensional hindered moisture absorption in polymeric composites: model development and validation. Polym Compos Jul 2013, 2008;34(7):1144–57.
[33] Akay M, Ah Mun SK, Stanley A. Influence of moisture on the thermal and mechanical properties of autoclaved and oven-cured Kevlar-49/epoxy laminates. Compos Sci Technol 1997;57(5):565.
[34] Rodriguez L, García C, Grace L. The effect of in-service aerospace contaminants on X-band dielectric properties of a bismaleimide/quartz composite. May 22, 2015.
[35] Garcia C, et al. Effects of moisture absorption on the dielectric properties of nanoclay-reinforced epoxy for radome applications. Nov 14, 2014. p. 1–7.
[36] Grace LR. The effect of moisture contamination on the relative permittivity of polymeric composite radar-protecting structures at X-band. Compos Struct 2015; 128:305–12.
[37] Koziol M, Figlus T. Evaluation of the failure progress in the static bending of GFRP laminates reinforced with a classic plain-woven fabric and a 3D fabric, by means of the vibrations analysis. Polym Compos Jun 2017, 2008;38(6):1070–85.
[38] Figlus T, Koziol M. Diagnosis of early-stage damage to polymer - glass fibre composites using non-contact measurement of vibration signals. J Mech Sci Technol Aug 01, 2016;30(8):3567–76.
[39] Ibarra-Castanedo C, et al. Nondestructive assessment of glass fibre composites by mid-wave and near infrared vision. Mater Trans 2012;53(4):601–3.
[40] Jolly M, et al. Review of non-destructive testing (NDT) techniques and their applicability to thick walled composites. Procedia CIRP 2015;38:129–36.
[41] Gholizadeh S. A review of non-destructive testing methods of composite materials. 2016. p. 50–7.
[42] Duchene P, et al. A review of non-destructive techniques used for mechanical damage assessment in polymer composites. J Mater Sci 2018;53(11):7915–38.
[43] Kapadia A. Non-destructive testing of composite materials. Handbook of Multiphase Polymer Systems 2011;1:777–96.
[44] Strobl M, et al. Advances in neutron radiography and tomography. Journal of Physics. D, Applied Physics Dec 21, 2009;42(21).
[45] Bossi RH, Giurgiutiu V. Nondestructive testing of damage in aerospace composites. Elsevier Ltd; 2015.
[46] Springer GS. Moisture content of composites under transient conditions. J Compos Mater 1977;11(1):107–23.
[47] Guha RD, Idolor O, Grace L. An atomistic simulation study investigating the effect of varying network structure and polarity in a moisture contaminated epoxy network. Comput Mater Sci 2020;179(January):109683.
[48] Guha RD, et al. Exploring secondary interactions and the role of temperature in moisture-contaminated polymer networks through molecular simulations. Soft Matter 2021;17(10):2942–56.
[49] Mijović J, Zhang H. Molecular dynamics simulation study of motions and interactions of water in a polymer network. J Phys Chem B 2004;108(8):2557–63.
[50] Zhang D, et al. Characteristics of water absorption in amine-cured epoxy networks: a molecular simulation and experimental study. Soft Matter Nov 07, 2018;14(43):874–8749.
[51] Tam L, Lau D, Wu C. Understanding interaction and dynamics of water molecules in the epoxy via molecular dynamics simulation. Mol Simulat 2018-11-01, 2019; 45(2):120.
[52] Guha RD, Idolor O, Grace L. Molecular dynamics (MD) simulation of a polymer composite matrix with varying degree of moisture: Investigation of secondary bonding interactions. 2019.
[53] Guha RD, et al. Temporal evolution of the behavior of absorbed moisture in a damaged polymer-quartz composite: a molecular dynamics study. Comput Mater Sci 2022;214:111690. https://doi.org/10.1016/j.commatsci.2022.111690. Available: https://www-sciencedirect-com.prox.lib.ncsu.edu/science/article/pii/S0927025622004177.
[54] Herrera-Gómez A, Velázquez-Cruz G, Martín-Polo MO. Analysis of the water bound to a polymer matrix by infrared spectroscopy. J Appl Phys May 15, 2001; 89(10):5431–7.
[55] Musto P, et al. Probing the molecular interactions in the diffusion of water through epoxy and epoxy-bismaleimide networks. Journal of Polymer Science. Part B, Polymer Physics May 15, 2002;40(10):922–38.
[56] Guha RD, et al. Consequences of humidity cycling on the moisture absorption characteristics of epoxy resins with different network architectures. ACS Appl Polym Mater 2023;5(1):400–11.
[57] O. Oluwajire et al., "Experimental validation of the dynamic molecular state of water in damaged polymer composites using near infrared spectroscopy," in American Society for Composites, Available: https://par.nsf.gov/servlets/purl/10411883.
[58] Hayward D, et al. The cure and diffusion of water in halogen containing epoxy/amine thermosets. Polymer 1997;38(5):1151.
[59] Pethrick RA, et al. Dielectric, mechanical and structural, and water absorption properties of a thermoplastic-modified epoxy resin: poly(ether sulfone)−Amine cured epoxy resin. Macromolecules Jul 15, 1996;29(15):5208–14.
[60] Idolor O, et al. 2-dimensional mapping of damage in moisture contaminated polymer composites using dielectric properties. 2019.
[61] Idolor O, Guha R, Grace L. A dielectric resonant cavity method for monitoring of damage progression in moisture-contaminated composites. 33rd Technical Conference of the American Society for Composites 2018;2:756–68.
[62] Idolor O, et al. Polymer-water interactions and damage detection in polymer matrix composites. Compos B Eng 2021;211.
[63] Idolor O, et al. An experimental study of the dynamic molecular state of transient moisture in damaged polymer composites. Polym Compos 2021.
[64] Idolor O, et al. Damage detection in polymer matrix composites by analysis of polymer-water interactions using near-infrared spectroscopy. 2020. p. 487–500.
[65] Johncock P, Tudgey GF. Epoxy systems with improved water resistance, and non-fickian behaviour of epoxy systems during water ageing. Br Polym J 1983;15(1): 14–8.
[66] Wang Z, et al. Simultaneously enhanced dielectric properties and through-plane thermal conductivity of epoxy composites with alumina and boron nitride nanosheets. Sci Rep 2021;11(1):1–11.
[67] Sarafis P, Nassiopoulou AG. Dielectric properties of porous silicon for use as a substrate for the on-chip integration of millimeter-wave devices in the frequency range 140 to 210 GHz. Nanoscale Res Lett Aug 21, 2014;9(1):418.
[68] R. A. Levy and R. J. Collier, Principles of solid state physics Elsevier, 196922(6).
[69] Maxwell ID, Pethrick RA. Dielectric studies of water in epoxy resins. J Appl Polym Sci Jul, 1983;28(7):2363–79.
[70] Fernández DP, et al. A database for the static dielectric constant of water and steam. J Phys Chem Ref Data Jan, 1995;24(1):33–70.
[71] Pethrick RA, et al. Effect of cure temperature on the structure and water absorption of epoxy/amine thermosets. Polym Int 1996;39(4):275.
[72] Anh Phuong Tran APT, Ardekani MRM, Lambot S. Coupling of dielectric mixing models with full-wave ground-penetrating radar signal inversion for sandy-soil-moisture estimation. Geophysics May 01, 2012;77(3):H33–44.
[73] Hallikainen MT, et al. Microwave dielectric behavior of wet soil-Part 1: empirical models and experimental observations. Tgrs Jan, 1985;GE-23(1):25–34.
[74] Berkowitz K, et al. Combined effects of impact damage and moisture exposure on composite radome dielectric properties. 2018.
[75] Patro S, et al. Artificial intelligence techniques for fault assessment in laminated composite structure: a review. E3S Web of Conferences 2021;309.
[76] Liu P, et al. Damage mode identification of composite wind turbine blade under accelerated fatigue loads using acoustic emission and machine learning. Struct Health Monit Jul, 2020;19(4):1092–103.
[77] Das S, Chattopadhyay A, Srivastava AN. Classifying induced damage in composite plates using one-class support vector machines. AIAA J Apr 01, 2010;48(4): 705–18.
[78] Dib G, et al. Ensembles of novelty detection classifiers for structural health monitoring using guided waves. Sms Jan 01, 2018;27(1):15003.
[79] Pawar PM, Nam Jung Sung. Support vector machine based online composite helicopter rotor blade damage detection system. J Intell Mater Syst Struct Oct 01, 2008;19(10):1217–28.
[80] Zargar SA, Yuan F. Impact diagnosis in stiffened structural panels using a deep learning approach. Struct Health Monit Mar, 2021;20(2):681–91.
[81] Lee IY, et al. Advanced non-destructive evaluation of impact damage growth in carbon-fiber-reinforced plastic by electromechanical analysis and machine learning clustering. Compos Sci Technol Feb 08, 2022;218:109094.
[82] Rahbari A, et al. Unsupervised damage clustering in complex aeronautical composite structures monitored by Lamb waves: an inductive approach. Eng Appl Artif Intell Jan, 2021;97.
[83] ASTM. ASTM D3171 Standard test methods for constituent content of composite materials. ASTM Standard; 2011.
[84] ASTM standard. ASTM D 5229– 92 – standard test method for moisture absorption properties and equilibrium conditioning of polymer matrix composite materials. Annu Book ASTM (Am Soc Test Mater) Stand 2010;92:1–13 *(Reapproved)*.
[85] Thorsson SI, Waas AM, Rassaian M. Low-velocity impact predictions of composite laminates using a continuum shell based modeling approach part A: impact study. Int J Solid Struct Dec 15, 2018;155:185–200.
[86] Derusova DA, et al. Evaluating impact damage in Kevlar/carbon composites by using laser vibrometry and active infrared thermography. Electron Lett Sep 17, 2020;56(19):1001–3.
[87] Malfense Fierro GP, Meo M. Nonlinear imaging (NIM) of barely visible impact damage (BVID) in composite panels using a semi and full air-coupled linear and nonlinear ultrasound technique. Nondestructive Characterization and Monitoring of Advanced Materials, Aerospace, Civil Infrastructure, and Transportation XII 2018;10599:22.
[88] Rodriguez LA, García C, Grace LR. Long-term durability of a water-contaminated quartz-reinforced bismaleimide laminate. Polym Compos 2018;39(8):2643–9.

[89] Grace LR, Altan MC. Three-dimensional anisotropic moisture absorption in quartz-reinforced bismaleimide laminates. Polym Eng Sci Jan 2014, 2006;54(1):137–46.
[90] Krupka J. Frequency domain complex permittivity measurements at microwave frequencies. Meas Sci Technol 2006;17(6).
[91] Krupka J. Precise measurements of the complex permittivity of dielectric materials at microwave frequencies. Mater Chem Phys 2003;79(2–3):195.
[92] Idolor O, et al. Nondestructive examination of polymer composites by analysis of polymer-water interactions and damage-dependent hysteresis. Compos Struct 2022;287:115377.
[93] Mohamad IB, Usman D. Standardization and its effects on K-means clustering algorithm. Res J Appl Sci Eng Technol 2013;6(17):3299–303.
[94] Kersemans M, et al. Non-destructive testing of composites by ultrasound, local defect resonance and thermography. Proceedings Jul 01, 2018;2(8):554.
[95] Berkowitz K, et al. Impact damage detection limits of microwave NDE technique for polymer composites. 2021. p. 2568–82.
[96] Bartley PG, Begley SB. A new free-space calibration technique for materials measurement. In: 2012 IEEE international instrumentation and measurement technology conference proceedings; 2012. p. 47–51.
[97] Wee FH, et al. Free space measurement technique on dielectric properties of agricultural residues at microwave frequencies. In: 2009 SBMO/IEEE MTT-S international microwave and optoelectronics conference (IMOC), (I); 2009. p. 183–7.
[98] Ghodgaonkar DK, Ali NA, Giubbolini L. Microwave nondestructive testing of composite materials using free-space microwave measurement techniques. In: 15th world conference on non-destructive testing; 2000. p. 1–6.
[99] Vetter TM, et al. Using infrared spectroscopy in combination with multivariate data analysis to predict residual strength of carbon fiber reinforced polymers after one-sided thermal loading. Polym Compos 2021;42(8):4138–41305.
[100] Gelabert P, et al. DLP NIRscan Nano: an ultra-mobile DLP-based near-infrared Bluetooth spectrometer. Emerging Digital Micromirror Device Based Systems and Applications VIII 2016;9761:97610B.
[101] Lorrain P, Corson DR. Electromagnetic fields and waves. 1970.
[102] Cole KC, Noël D, Hechler J-. Applications of diffuse reflectance fourier transform infrared spectroscopy to fiber-reinforced composites. Polym Compos Dec, 1988;9(6):395–403.
[103] Yu B, et al. A comparison of different approaches for imaging cracks in composites by X-ray microtomography. Phil Trans Math Phys Eng Sci 2016;374.